



Supporting Online Material for

Isotopic Compositions of Cometary Matter Returned by Stardust

Kevin D. McKeegan,^{*} Jerome Aléon, John Bradley, Donald Brownlee, Henner Busemann, Anna Butterworth, Marc Chaussidon, Stewart Fallon, Christine Floss, Jamie Gilmour, Matthieu Gounelle, Giles Graham, Yunbin Guan, Philipp R. Heck, Peter Hoppe, Ian D. Hutcheon, Joachim Huth, Hope Ishii, Motoo Ito, Stein B. Jacobsen, Anton Kearsley, Laurie A. Leshin, Ming-Chang Liu, Ian Lyon, Kuljeet Marhas, Bernard Marty, Graciela Matrajt, Anders Meibom, Scott Messenger, Smail Mostefaoui, Sujoy Mukhopadhyay, Keiko Nakamura-Messenger, Larry Nittler, Russ Palma, Robert O. Pepin, Dimitri A. Papanastassiou, François Robert, Dennis Schlutter, Christopher J. Snead, Frank J. Stadermann, Rhonda Stroud, Peter Tsou, Andrew Westphal, Edward D. Young, Karen Ziegler, Laurent Zimmermann, Ernst Zinner

^{*}To whom correspondence should be addressed. E-mail: mckeegan@ess.ucla.edu

Published 15 December 2006, *Science* **314**, 1724 (2006)
DOI: 10.1126/science.1135992

This PDF file includes:

Methods
Figs. S1 to S5
Tables S1 to S6

Isotopic compositions of cometary matter returned by STARDUST

Samples and Methods

A wide variety of Wild2 sample types were probed by several analytical tools to provide a preliminary characterization of the range of isotope effects present. Spot analyses of H, C, N, and O isotopes were performed by secondary ion mass spectrometry (SIMS) on entire particle fragments (typically ~2 – 10 μm) extracted from aerogel collector blocks and pressed into clean gold foil. Such “bulk” analyses tend to yield the highest precision, but may average over any isotope heterogeneities existing on a very fine spatial scale, and in some cases, also suffer from contamination by compressed aerogel adhering to the periphery or even intimately mixed with the comet particle. Data on whole particle fragments are suitable for comparison to spectroscopic data (IR, Raman) acquired with similar resolution and with mineralogy/petrology at the scale of the scanning electron microscope. Much higher spatial resolution is achieved by NanoSIMS analysis, which uses a primary ion beam <100 nm in diameter rastered over the sample surface to produce elemental and isotopic “maps”. NanoSIMS analyses typically realize worse precision but clearly discriminate against aerogel contamination and can also be used to identify sub-micron circumstellar dust grains amidst more normal (i.e., solar system-like) materials by virtue of their potentially large isotope anomalies.

Hydrogen isotopic measurements

Hydrogen isotopes were measured along with carbon using a Cameca ims-6f ion microprobe at the Carnegie Institution of Washington, in scanning imaging mode. A focused <10pA Cs^+ ion beam was rastered across samples with synchronized collection of secondary ions. Techniques were identical to those described in (S1). All but one analyzed sample were extracted from the aerogel collectors and pressed into Au foils. A 500 nm thick slice of sample Track 13 (FC9,0,13,1,0) prepared by ultramicrotome, was placed directly on a Au foil. Data were quantified using custom image processing software and terrestrial standards.

Table S1. D/H ratios measured in Stardust samples (1σ errors)

Sample	$\delta\text{D}/\text{H}$ (‰)	D/H ($\times 10^6$)
Track 13	900 \pm 350	296 \pm 55
Track 35,25 (bulk)	633 \pm 119	254 \pm 19
Sub-region	1899 \pm 1057	451 \pm 165
Sub-region	2243 \pm 984	505 \pm 153
Sub-region	1394 \pm 839	373 \pm 131
Sub-region	917 \pm 542	299 \pm 84
Track 35,27	-238 \pm 130	119 \pm 20
Track 2	176 \pm 115	183 \pm 18
Track 17	1655 \pm 676	413 \pm 105

Noble gas analysis of bulbous particle tracks in Stardust aerogel: a search for volatiles

Noble gases were measured in blank aerogel chips, flown aerogel chips and two fragments of bulbous aerogel at the CRPG in Nancy, France. The first piece had material

from the wall of a large bulbous track (c2044,0,41; tile 44, track 7; hereafter, "Thera1"). This sample together with blank and flown samples were analysed during a first session on 12-15 June, 2006 after extensive blank determination. Given the results of this first trial, we were supplied with a second, larger, piece of the same wall, referred here as "Thera 2". This sample was analysed together with another piece of flown aerogel on 11-13 July, 2006.

Samples were handled in a clean room (class 10,000 in the room, class 100 in extraction boxes) under a microscope using a clean single-hair paintbrush attached to a manipulator. It was not possible to weigh aerogel chips due to their small size, and we have estimated the mass from optical measures of the surface area of the chips (assuming that all chips have a comparable thickness). Samples were loaded in pits of the laser chamber and connected to a high vacuum line developed for the analysis of ET samples. Samples were outgassed at 80°C (Thera 1 run) and 100°C (Thera 2 run) overnight and left pumping (1.5×10^{-9} mbar) at room temperature for 3 weeks (Thera 1) and 1 week (Thera 2).

Chips were heated using a CO₂ infrared ($\lambda = 10.6 \mu\text{m}$) laser mounted on a x-y stage and monitored through a microscope equipped with a CCD camera. A visible (He-Ne) laser was used to align the IR laser and we discovered that even the weak pointer laser was provoking vibrations of the chips under illumination. Hence we heated the chips with great care by increasing very slowly the power of the CO₂ laser in order to avoid sample jumping out of the pits. We lost one blank aerogel sample and thus we did not analyse other small blank aerogel samples. Fortunately, the flown aerogel chips and the bulbous chips were bigger and could be safely analysed. Once thermal coupling of the aerogel sample with the laser beam was achieved, aerogel chips could be totally molten. Gases were purified over two titanium getters and analysed with a VG5400 static mass spectrometer following methods presented elsewhere (S2). Analytical blanks (without laser heating and with laser heating of a metal surface adjacent to the samples) were thoroughly investigated and analyses started only when the blanks were indistinguishable to those of the purification line alone, as determined during several months prior to these experiments. The blanks (n= 6) were $4.9 \pm 2.9 \times 10^{-15}$ mol, $0.86 \pm 0.20 \times 10^{-15}$ mol, and $0.11 \pm 0.03 \times 10^{-15}$ mol for ⁴He, ²⁰Ne and ³⁶Ar, respectively (Table 1).

Results (Table S2) suggest that aerogel chips containing bubbles and cometary particle fragments have excesses of helium and neon relative to the blanks. For argon, all measurements were within the range of blank values and are not discussed further. We found no relationship between the aerogel surface area and the amount of extracted gas, for both helium and neon. Extractions of flown aerogel without bubbles are comparable to the blanks, given uncertainties. This suggests strongly that the instrumental blank dominates over the aerogel blank for the sample size we analysed. Therefore, an upper limit of the aerogel blank is given by instrumental blanks (Table S2).

Both Thera 1 and Thera 2 show excesses of He and Ne relative to blank levels. A possible exception is helium extracted from Thera 2 which is close to the amount of He extracted from the unexposed flight aerogel #1. Unfortunately, ³He could not be analysed with confidence due to the low He amount and the mass spectrometer setting, which was a compromise (trap current of 200 μA , electron energy of 65 eV) made to analyse He, Ne and Ar together.

Data reduction for Ne isotopic ratios required correction for significant blank contribution, which was done by subtracting from either Thera 1 or Thera 2 data the respective flown aerogel (runs #1 & #2). When propagating errors, we considered that standard deviations of repeated blank measurements were representative of blank correction uncertainties and adopted these as errors on blank measurements. During the Thera 1 run, the analyser electronics had a drift problem which resulted in increasing the uncertainty on the $^{20}\text{Ne}/^{22}\text{Ne}$ ratio.

Table S2: He and Ne data in aerogel samples. Abundances are in units of 10^{-15} mol

Sample	area mm ²	⁴ He	+/-	²⁰ Ne	+/-	²⁰ Ne/ ²² Ne/	+/-	²¹ Ne/ ²² Ne	+/-
Instrumental blank (n= 6)		4.9	2.9	0.86	0.20	9.68	0.24	0.0210	0.0130
blank flight aerogel #1	0.42	12.4	7.3	1.17	0.27	9.64	0.36	0.0243	0.0023
c2044,0,41; tile 44, track 7, "Thera 1"	0.26	36.0	2.0	2.27	0.11	10.97	1.12	0.0243	0.0024
Thera 1 corrected for blank		23.6	7.6	1.10	0.29	12.86	3.20	0.0245	0.0029
blank flight aerogel #2	0.06	2.8	1.7	1.03	0.05	9.35	0.11	0.0305	0.0011
c2044,0,41; tile 44, track 7, "Thera 2"	0.30	10.6	0.53	3.61	0.18	10.14	0.12	0.0293	0.0011
Thera 2 corrected for blank		7.8	1.7	2.58	0.19	10.49	0.24	0.0279	0.0017
Air						9.80		0.0292	
Solar						13.8		0.0330	

In a $^{22}\text{Ne}/^{20}\text{Ne}$ versus $^4\text{He}/^{20}\text{Ne}$ mixing diagram (Fig. S1), data appear significantly different from the atmospheric values and are most consistent with a cometary end-member having a solar Ne isotopic composition (although the data do not allow one to constrain other potential ET end-members) and a $^4\text{He}/^{20}\text{Ne}$ ratio of about 20, the mixing line constructed with this value fitting best the two data points (Fig. S1).

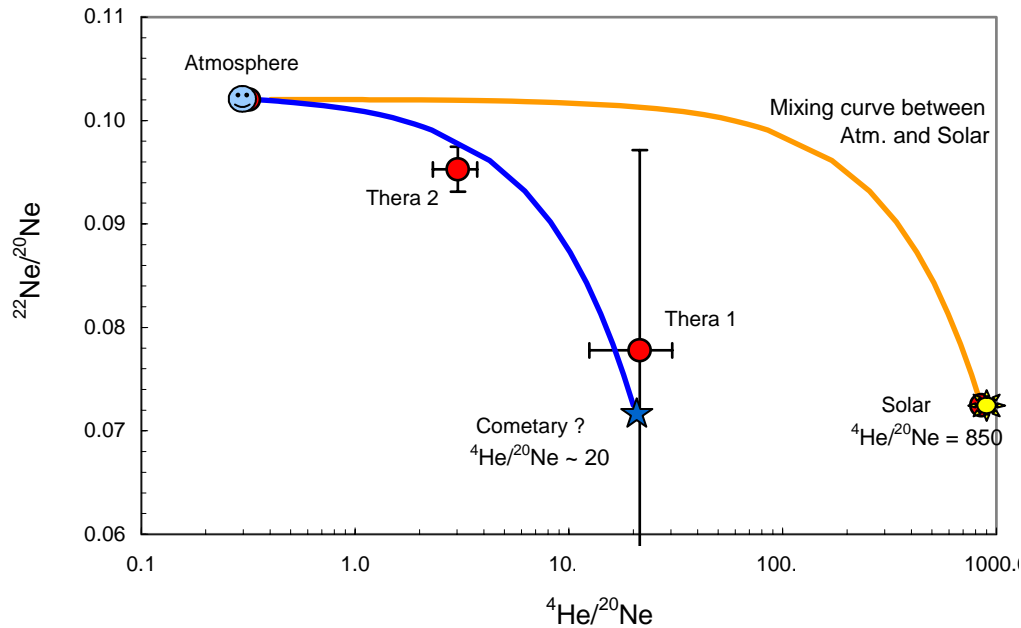


Figure S1: The $^{20}\text{Ne}/^{22}\text{Ne}$ ratio as a function of the $^4\text{He}/^{20}\text{Ne}$ ratio. The black curve represents mixing between the atmospheric component and the Solar component, and the blue curve is mixing between the atmosphere and a component having a solar $^{20}\text{Ne}/^{22}\text{Ne}$ ratio and a $^4\text{He}/^{20}\text{Ne}$ ratio of 20 and was adjusted to fit the two data points.

Crater residue measurements

Impact residues in and around 4 large craters (59 - 370 μm) in Al foil strips were studied for C-, N-, and O-isotopic compositions by high-resolution ion imaging with Cameca NanoSIMS 50 ion microprobes at Washington University, St. Louis and at the Max-Planck-Institute for Chemistry, Mainz. In addition, residues in 37 small craters (0.32-1.5 μm) were measured for O-isotopic compositions and residues in another 6 small craters (0.61-1.9 μm) were analyzed for C- and N-isotopic compositions. The measurements followed the specific procedures developed for Stardust-analogue samples (S3). Results are summarized in tables S3 (oxygen) and S4 (carbon, nitrogen).

Table S3. Oxygen isotopic characteristic of crater residues analyzed by NanoSIMS isotope mapping.

Sample	Size (μm)	Bulk $\delta^{17}\text{O}$ (‰)	Bulk $\delta^{18}\text{O}$ (‰)	Presolar Grains?
<i>Large craters</i>				
Al foil C2013N	140	*	*	No
Al foil C2086N	59	*	*	No
Al foil C2118N	72	*	*	No
Al foil C2086W	~370	*	*	Yes (1)
<i>Small craters</i>				
37 craters (Al foils C2044W, C2052N)	0.32 – 1.5	-9 \pm 10	-10 \pm 5	No

* No bulk data available because no (near-by) external standard was measured.

Quoted errors are 1σ , based on counting statistics. Additional systematic uncertainties of 1-2% should be applied due to QSA correction, O-isotopic composition of contamination on the Al foil which was used for normalization, matrix effects, reproducibility of ratio measurements.

Table S4. Carbon and Nitrogen isotopic characteristics of crater residues measured by isotope mapping in the NanoSIMS.

Sample	Size (μm)	Bulk $\delta^{13}\text{C}$ (‰) ¹	Bulk $\delta^{15}\text{N}$ (‰) ¹	Presolar Signatures?
<i>Large craters</i>				
Al foil C2013N	140	-25 \pm 1	451 \pm 7	¹⁵ N enrichment
Al foil C2086N	59	-21 \pm 1	-11 \pm 3	No
Al foil C2118N	72	²	²	No ³
Al foil C2086W	~370	²	²	No
<i>Small craters</i>				
#56 (Al foil C2037N)	1.9	-7 \pm 8	266 \pm 47	¹⁵ N enrichment
5 craters (Al foil C2037N)	0.61 – 1.3	-12 \pm 9	98 \pm 53	No

¹ The C- and N-isotopic data were normalized to measurements on nearby C- and N-rich contamination. Errors are 1σ . Systematic uncertainties due to matrix and topographic effects are estimated to be 1-2 % for C and several % for N.

² No bulk data available because no (near-by) external standard was measured.

³ One candidate grain with a ^{15}N depletion sputtered away during analysis.

Oxygen isotope analyses of STARDUST grains

High precision oxygen isotope analyses were made using the Cameca ims 1270 instruments at the Centre de Recherches Pétrographiques et Géochimiques, Nancy, and at the University of California, Los Angeles. The enstatite grain (T69) was embedded in acrylic, ultra-microtomed, extracted from acrylic using acetone, transferred and pressed onto gold foil. Some fragments of acrylic were still present around the grains and the acrylic had been annealed locally by the electron beam used to perform electron microprobe analyses. No additional cleaning was performed on the grain before the introduction of the gold foil in the ion microprobe. The forsterite-rich grain (T22) was extracted from aerogel using a fine needle, and then pressed into clean gold foil. No attempt was made to remove adhering aerogel. The refractory particle "Inti" was potted in acrylic for ultramicrotomy and the remainder of the cut section was cut off and pressed into In and coated with a thin layer of Au for ion probe analysis.

Isotopic measurements were made by sputtering with a 20keV, $\sim 0.1 - 0.2$ nA Cs^+ beam. Spot size was about $\sim 8-10$ μm for the analyses of T22 and T69 and the first run on Inti; for the second set of analyses on Inti the beam was better focused to ~ 5 μm resulting in essentially no overlap with aerogel adhering to the particle, but still incorporating a mixture of mineral phases from the particle. For all analyses, low-energy negative secondary ions were accelerated to 10 keV and analyzed at high resolving power ($m/\Delta m > 6500$) in order to separate all interfering molecular species ($^{16}\text{OH}^-$, $^{17}\text{OH}^-$, $^{16}\text{OH}_2^-$) from atomic oxygen ions and a normal-incidence electron gun was utilized for charge compensation. A Faraday cup (FC) detector was used to measure $^{16}\text{O}^-$ current, while the ion beams for the minor isotopes ^{17}O and ^{18}O were measured by pulse counting with electron multipliers (EM). Ion intensities were corrected for background (FC) and deadtime (EM). Instrumental mass fractionation (IMF) and relative detector efficiencies were corrected by comparison to measurements made on terrestrial standards (mantle olivine and pyroxene, as well as hibonite and spinel) interspersed with those of the unknowns; "matrix effects" in the instrumental mass fractionation are known to be small for this suite of minerals. Quoted uncertainties are 2 standard error of the mean and incorporate external reproducibility on standards.

One analysis was made on acrylic fragments which are present in the vicinity of the enstatite grain T69 to evaluate possible contamination from the acrylic during the analysis. The measured $\delta^{17}\text{O}$ (-19.5 ± 1.2 ‰) and $\delta^{18}\text{O}$ (-33.5 ± 0.5 ‰) are very negative (when corrected with instrumental mass fractionation determined on enstatite) probably reflecting large matrix effects on instrumental mass fractionation (although the oxygen isotope composition of the acrylic is not known). Oxygen emissivity from the acrylic was high (on the order of a factor of 20% to 50% of the signal from silicates) so that its contribution to the total O signal cannot be neglected.

Six analyses were made on the enstatite grain (T69) at different locations on the grain (Table S5). The positions of the spot were chosen in order to try to maximize the

count rate on oxygen, while minimizing overlap of the beam with acrylic. The measured oxygen isotope composition show a range of variations (Fig S2, Table S4) which most likely reflects the mixing under the ion probe beam of various proportions of enstatite and acrylic. The 3 analyses which show minimal mixing effects are plotted in Fig. 4; all analyses are shown in Fig. S2. The two analyses of a forsterite grain (T22) show minimal contamination from adhering aerogel.

Table S5. Oxygen isotopic compositions of comet 81P/Wild2 grains.

Sample	$\delta^{18}\text{O}$ (‰)	$\delta^{17}\text{O}$ (‰)	phases analyzed / comments
<u>C2115,1,22,0 (Track 22):</u>			
spot 1	-1.7 ± 1.2	-1.5 ± 1.6	10 μm grain; Mg-rich olivine with
spot 2	2.2 ± 1.2	0.4 ± 1.7	minor pyroxene
spot 3	-6.0 ± 1.1	-2.6 ± 1.7	affected by aerogel contamination
<u>C2027,2,69,1,0 (Track 69):</u>			
run 1, spot 1	-0.3 ± 0.4	-0.8 ± 0.9	low-Ca pyroxene
run 1, spot 2	4.5 ± 0.4	-0.1 ± 0.9	
run 2, spot 1	1.1 ± 0.4	-1.1 ± 1.1	
	-5.2 ± 0.6	-3.8 ± 1.7	acrylic contamination evident
	-6.9 ± 0.5	-4.9 ± 1.2	acrylic contamination evident
	-8.8 ± 0.8	-6.8 ± 1.7	acrylic contamination evident
<i>Acrylic embedding medium</i>			
	-33.5 ± 0.5	-19.5 ± 1.2	Not properly normalized; measured composition reflects large instrumental mass fractionation
<u>C2054,4,25,1,0 (Track 25, "Inti"):</u>			
run 1, spot 1	-39.5 ± 1.0	-39.4 ± 4.3	10 μm refractory particle
run 1, spot 2	-36.1 ± 2.4	-38.7 ± 3.8	some aerogel contamination possible
run 2, spot 1	-40.9 ± 1.3	-40.5 ± 1.6	mix of melilite, anorthite, and spinel
run 2, spot 2	-41.6 ± 1.3	-42.0 ± 2.5	(S4)

A variety of samples were also analyzed for C, N and O isotope compositions using the Cameca NanoSIMS 50 at the Lawrence Livermore National Laboratory. Isotope abundances were determined by quantitative ion imaging using a ~ 0.6 to 1.2 pA, 16 keV $^{133}\text{Cs}^+$ primary ion beam focused into a ~ 100 nm spot and rastered over areas ranging in size from 4×4 to 13×13 μm^2 , depending on the size of the sample and extent of contamination by aerogel or acrylic. An electron flood gun was used to provide charge compensation for O-isotope analyses of some samples. Scan rates were variable, depending on image size and secondary intensity, with dwell times of 1 to 5 ms per pixel. Secondary ion intensities for $^{12}\text{C}^-$, $^{13}\text{C}^-$, $^{16}\text{O}^-$, $^{17}\text{O}^-$, $^{18}\text{O}^-$, $^{12}\text{C}^{14}\text{N}^-$, and $^{12}\text{C}^{15}\text{N}^-$, together with secondary electrons, were collected simultaneously (5 species at a time) in multi-collection mode at a mass resolving power of ~ 6500 , sufficient to separate $^{13}\text{C}_2$ from $^{12}\text{C}^{14}\text{N}$, and $^{12}\text{C}^{15}\text{N}$ from $^{13}\text{C}^{14}\text{N}$. Three difference sequences of masses were measured: ^{16}O , ^{17}O , ^{18}O and ^{28}Si for O-isotopes; ^{16}O , ^{17}O , ^{18}O , $^{12}\text{C}^{14}\text{N}$ and $^{12}\text{C}^{15}\text{N}$ for O and N isotopes; and ^{12}C , ^{13}C , ^{16}O , $^{12}\text{C}^{14}\text{N}$ and $^{12}\text{C}^{15}\text{N}$ for C and N isotopes; secondary electron

images were collected with each sequence. The isotope imaging measurements consist of 40 to 100 scans over each region of interest; the scans are subsequently added together to create a single image for each area. The data are processed as quantitative isotope ratio images using custom software. Isotope ratio images are obtained by dividing the images of two species, e.g., ^{12}C and ^{13}C , pixel by pixel, and are corrected for image drift and statistical outliers. Typically, the data are smoothed using a 4×4 pixel² integration area. The C, N, and O isotope ratios measured in Stardust samples are calibrated to ratios measured in standards: NIST SRM-24 graphite for C, NIST SRM-8558 KNO₃ embedded in SRM-24 graphite and Mahakam Delta 48055 type III kerogen crushed on gold for N, and aerogel for O. The NanoSIMS O-isotope data reported here were renormalized to the ims-1270 data for “Inti” to correct for mass-dependent fractionation. The normalized ratios are reported using delta notation (permil deviation from the appropriate standard). Uncertainties in isotope ratios are reported as 2 standard deviations and include counting statistics errors on individual measurements propagated with the reproducibility of replicate measurements of the standards.

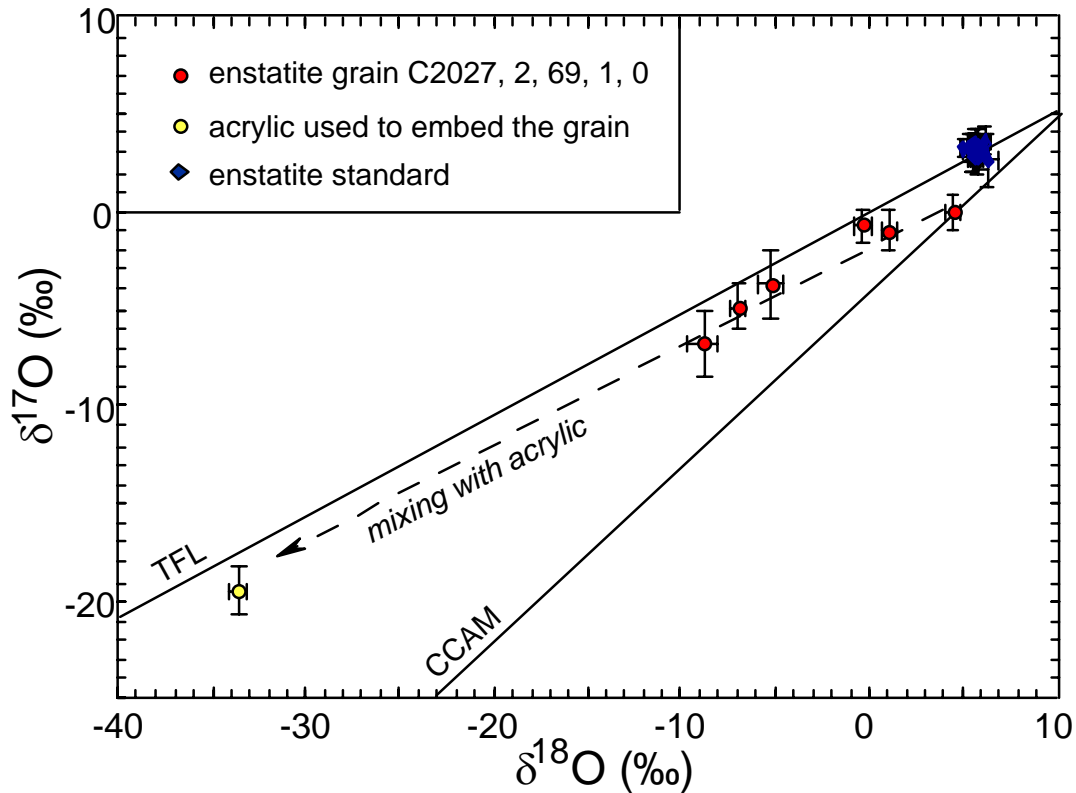


Figure S2. Three oxygen isotopes diagram showing the composition of the six spots made on Stardust enstatite grain C2027, 2, 69, 1, 0 (Track 69). The terrestrial fractionation line (TFL) and the carbonaceous chondrites anhydrous minerals line (CCAM) are shown for reference. The range of variation observed is likely due to mixing under the ion probe beam with fragments of acrylic used to embed the grain. The least contaminated spot lies on the CCAM line.

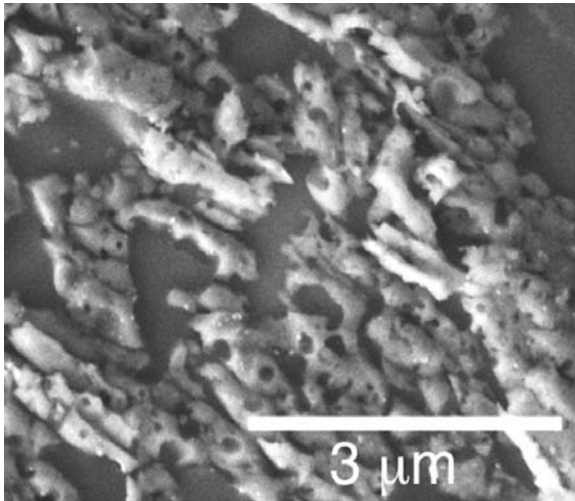


Fig. S3. Secondary electron image of a microtomed slice of particle C2025W showing vesicular glass embedded in epoxy (smooth areas). Numerous, small sulfide inclusions are visible entrained in glass.

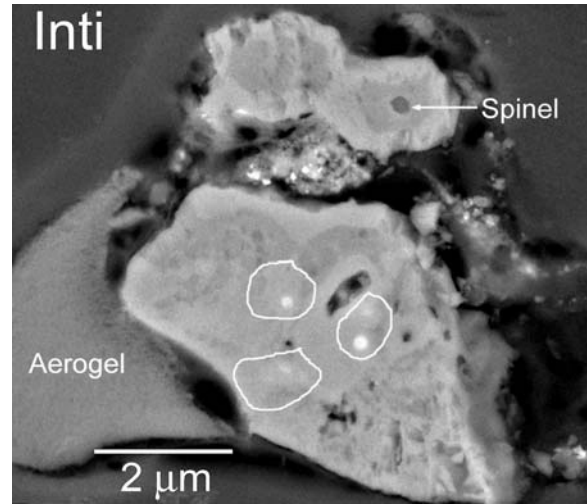


Fig. S4. Secondary electron image of a polished fragment of the refractory inclusion Inti; see Zolensky et al. (S4) for a discussion of the mineralogy. Areas analyzed for O-isotopes are outlined.

O-isotope abundances were measured in 4 microtomed slices (serial sections) of a fine-grained “particle” consisting of Mg-rich vesicular glass containing numerous sulfide inclusions and in two microtomed slices of the “Inti” refractory inclusion (Figs. S3, S4); a polished “thick” section of Inti was subsequently analyzed with the ims-1270 at UCLA. O-isotope ratio images of 4 sections of vesicular glass show no evidence for isotope heterogeneity within a measurement precision of 4-6% at the 200 nm spatial scale. The average composition defined from 7 isotope ratio images reveals a composition consistent with average chondritic material and plots along the terrestrial fractionation (TF) line with $\delta^{17}\text{O} = 4 \pm 12\text{‰}$ and $\delta^{18}\text{O} = 9 \pm 7\text{‰}$. In contrast, the O-isotope ratio images of “Inti” show clear evidence of ^{16}O enrichment and define a composition plotting along the CCAM line with $\delta^{17}\text{O} = -62 \pm 20\text{‰}$ and $\delta^{18}\text{O} = -42 \pm 10\text{‰}$ (Fig. S5). The relationship seen here between mafic silicates with $\Delta^{17}\text{O} \sim 0\text{‰}$ and Ca-Al-rich refractory material with $\Delta^{17}\text{O} \sim -40\text{‰}$ is strikingly similar to that observed in carbonaceous chondrites.

Nitrogen and carbon isotope analyses

N- and C-isotope abundances were measured in the fine-grained vesicular glass described in the preceding paragraph. The C and N secondary ion signals are both very low, reflecting the low abundance of carbon in the glass. Based on the $^{12}\text{C}^-/^{14}\text{N}^-$ ratio, we estimate the N abundance as ~ 900 ppm. This N concentration is 10 to 100 times lower than that found in D-rich and ^{15}N -rich organic material from chondritic IDPs. Due to the low abundances, differentiating C and N indigenous to Stardust material from terrestrial contamination is challenging. The carbon isotope abundances are indistinguishable from normal terrestrial material. Nitrogen, in contrast, exhibits anomalous isotope abundances both on the scale of the whole particle, $\delta^{15}\text{N} = 108 \pm 10 \text{‰}$, and in isolated “hotspots”

with sizes of ~200 to 800 nm; $\delta^{15}\text{N}$ values for 82 localized regions range from -260‰ to +970‰. ^{15}N -enriched regions are more prevalent and the weighted mean $\delta^{15}\text{N}$ of all 82 hotspots is 320 ± 24 ‰. The range of $\delta^{15}\text{N}$ values is similar to that observed in chondritic IDPs (S5). The ^{15}N excesses appear to be associated with carbonaceous material characterized by C and N concentrations equal to or lower than those found in typical kerogens.

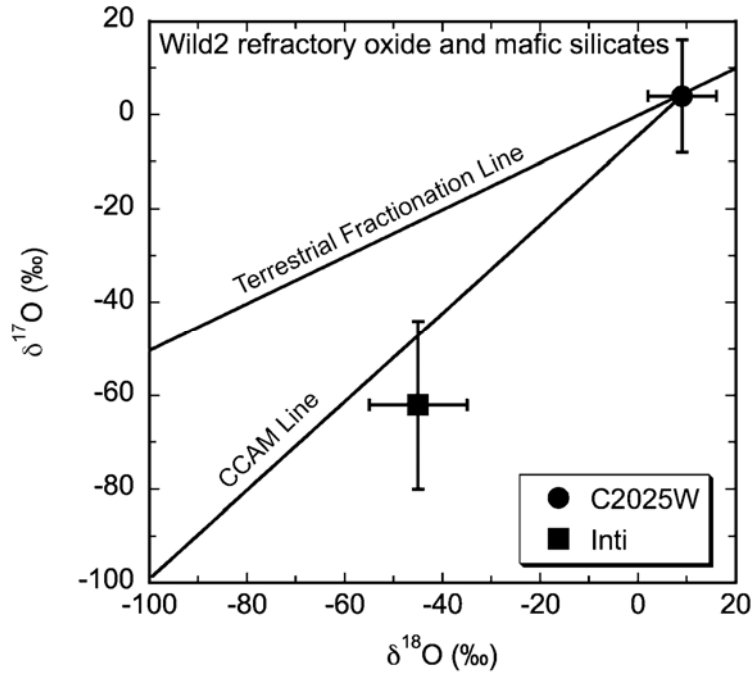


Fig. S5. Oxygen isotope compositions of refractory inclusion “Inti” and Mg-rich vesicular glass, determined by NanoSIMS. Inti is enriched in ^{16}O , similar to refractory inclusions in chondritic meteorites, while the vesicular glass has a composition similar to mafic silicates in carbonaceous chondrites. Uncertainties are 2σ .

Oxygen isotopic composition of aerogel

The oxygen isotope composition of flight aerogel was determined by laser-assisted fluorination mass spectrometry at UCLA. Stardust silica aerogel sample b#40, 2393-911 was cut by a razor blade and weighed into 1-2 mg-sized chunks, placed in a small open box (Au-foil), and kept dry overnight in a 60°C oven. The box was introduced into the reaction chamber of a vacuum fluorination line under dry nitrogen gas flow. The reaction chamber was evacuated until a vacuum of better than 1×10^{-6} mbar was achieved. The sample chamber was then continuously pumped for 2 days, during half of which it was externally heated (IR-lamp) to 50°C .

Fluorination of crystalline material requires that the evacuated reaction chamber and samples are pretreated with an aliquot of F_2 , usually overnight. This is to ensure that any contamination introduced into the chamber during sample insertion will react with F_2 , and then be pumped away. However, due to the high surface area of the silica aerogel,

and its extreme reactivity, this step led to partial reaction of the F₂ with the aerogel test samples, liberating oxygen prior to the actual laser-fluorination. Tests showed that the extended evacuation and heating to 50°C is sufficient to achieve the same low levels of contamination afforded by F₂-pretreatment.

Laser-fluorination was carried out using a 25 W CO₂ laser that heats the sample in an atmosphere of 50 mbar purified F₂. Excess F₂ was removed by reaction of the O₂/F₂ mixture with KBr. The oxygen was then purified by absorption on a 13X molecular sieve at -190°C, followed by elution of the O₂ from the first sieve at -131°C to a second 5A molecular sieve at -190°C. This step removes trace amounts of NF₃ by retention on the first sieve, permitting separation of O₂ and NF₃ and ensuring that the analyte O₂ is free from interferences that compromise the accuracy of Δ¹⁷O measurements (NF⁺ is an isobar for ³³O₂⁺ on the gas-source mass spectrometer). The oxygen was then admitted directly to a Finnigan DeltaPlus dual inlet isotope ratio mass spectrometer for measurement of the isotope ratios. Each sample gas was analyzed multiple times (n in Table S6), each analysis consisting of 20 cycles of sample-standard comparison.

The oxygen isotope ratios are calibrated against the isotopic composition of air O₂ and San Carlos olivine. For tropospheric oxygen we obtain δ¹⁸O and δ¹⁷O values of 23.51 ± 0.01 ‰ and 11.97 ± 0.03 ‰ respectively (the negative Δ¹⁷O of tropospheric air relative to rocks is well known). A typical analysis of San Carlos olivine in our lab gives δ¹⁸O = 5.32 ± 0.01 ‰ and δ¹⁷O = 2.75 ± 0.04 ‰.

Table S6: oxygen isotopic composition of flight aerogel

date	wt. (mg)	yield** (%)	δ ¹⁷ O'		δ ¹⁸ O'		Δ ¹⁷ O'		n
			mean	st.dev.	mean	st.dev.	mean	st.dev.	
12-Aug-06	1.21	86	-0.462	0.033	-0.987	0.026	0.060	0.029	7
16-Aug-06	1.91	72	-0.571	0.017	-1.184	0.020	0.055	0.023	12
		average	-0.516		-1.086		0.057		
		st.dev.	0.077		0.139		0.003		

* pressure of sample O₂-gas in mass spectrometer bellow

** aerogel yield estimated by assuming a SiO₂ formula unit.

References and Notes

- S1. H. Busemann *et al.*, *Science* **312**, 727 (May, 2006).
- S2. B. Marty, P. Robert, and L. Zimmermann, *Meteoritics and Planetary Science* **40**, 881 (2005).
- S3. P. Hoppe *et al.*, *Meteoritics and Planetary Science* **41**, 197 (2006).
- S4. M. E. Zolensky *et al.*, *Science*, this volume.
- S5. J. Aléon, F. Robert, M. Chaussidon, B. Marty, *Geochimica et Cosmochimica Acta* **67**, 3773 (Oct, 2003).